

International Conference on Space Optics—ICSO 2020

Virtual Conference

30 March–2 April 2021

Edited by Bruno Cugny, Zoran Sodnik, and Nikos Karafolas



Reaching GHz single photon detection rates with HgCdTe avalanche photodiodes detectors



Reaching GHz single photon detection rates with HgCdTe avalanche photodiodes detectors

S. Pes^{*a}, J. Rothman^{‡a}, P. Bleuet^a, J. Abergel^a, S. Gout^a, P. Ballet^a, J.-L. Santailier^a, J.-A. Nicolas^a,
J.-P. Rostaing^a, S. Renet^a, A. Vandenberg^a, L. Mathieu^a, J. Le Perche^a

^a Univ. Grenoble Alpes, CEA, Leti, F-38000 Grenoble, France

*salvatore.pes@cea.fr; ‡johan.rothman@cea.fr

ABSTRACT

In the present communication, the characterization results of an in-house developed four-quadrants detection module based on HgCdTe APDs and a Si-CMOS ROIC pre-amplifier is discussed. The module has been designed to be employed as high data rate ground-segment detector for 1.55 μm long-distance free-space optical communication links in the framework of a project funded by the European Space Agency. The detector is characterized by a multiplication gain in excess of $M = 150$, a ROIC input referred noise of $N_e = 45$ electrons rms and a measured bandwidth of $BW = 450$ MHz. These characteristics enable the linear-mode detection of meso-photon states ranging from tens of photons per pulse down to the single-photon level at high count rates exceeding 500 MHz per quadrant (and 2 GHz if the signal is dispatched over all four-quadrants).

For the present module, the performance for PPM and OOK modulation formats was estimated and its potentiality for long-distance free-space optical communications employing these modulation formats was validated. In particular, for the PPM format, a detection probability of 0.9 and a false alarm probability of 10^{-2} , a minimum PPM slot width of 500 ps and a temporal jitter with a $FWHM \sim 160$ ps were estimated, for an incident photonic state with 10 photons/pulse. The potentiality of the detector for 625 Mbps OOK modulation format was also evaluated and compared with a quantum limited situation. In this case, a -3.9 dB penalty from the quantum limited BER was obtained. A new generation of detectors is currently in development, which is expected to further improve the performance.

Keywords: linear-mode HgCdTe APDs, avalanche photodiodes, single photon detectors, meso-photon state detection, high detection rates, free-space optical communications, Pulse-Position Modulation, On-Off Keying modulation

1. INTRODUCTION

The high gain and the low excess noise factor are key advantages of HgCdTe avalanche photodiodes (APDs), which allows the detection of optical signals down to the single photon level with a detection efficiency expected to exceed 90%. When operated in linear mode, these detectors preserve a high dynamic range, which enables the detection of multi-photon states, and do not exhibit a dead time after each detection event. This also implies that the detection rate is only limited by the bandwidth of the APD and the pre-amplifier circuit, meaning that detection rates in excess of 1 GHz can be achieved with such detectors, surpassing other single photon detection technologies by a factor 10 to 1000 [1,2]. Such high-count rates make HgCdTe APDs interesting candidates for high data rate classical free-space optical communications (FSO) [3-5], quantum communications [6], and astronomy [7].

Concerning their applications in long-distance free-space communications, previous use of detector modules based on linear-mode HgCdTe APDs include:

- a 2×8 pixel detector by DRS Technologies in the framework of the NASA's sponsored In-space Validation of Earth Science Technologies (InVEST) program [3,8]. For such detector a single-pixel data rate of 50 Mbps and a multi-pixel array data rate of 110 Mbps at 1550 nm were reported;

- a detector module by CEA-Leti employed as ground detector to demonstrate the ESA Lunar Optical Communications Link (LOCL) between NASA's Lunar Atmosphere and Dust Environment Explorer (LADEE) spacecraft and ESA's Optical Ground Station (OGS) on the Canary Island [9]. This latter demonstration was able to support a downlink transmission from LADEE at a data rate of 71.1Mbps at 1550 nm.

Increasing the bandwidth of the detector directly translates into an improvement of the transmission data rate.

In this regard, the GHz single photon rate landmark has been recently approached at CEA-Leti by the development of a ground-segment detection module for 1.55 μm long-distance free-space optical communications in collaboration with the European Space Agency. The detection module consists of a four-quadrants HgCdTe APDs, designed to minimize the collection time of the photo-generated carriers, and a dedicated Si-CMOS readout integrated circuit, designed to achieve high bandwidth and low noise level. With such a module, single photon detection has been recently demonstrated up to count rates of 500 MHz [10], implying a cumulative detection rate of 2 GHz if the signal is dispatched over all four-quadrants.

The aim of this communication is to discuss the performance of HgCdTe APDs at GHz count rates in perspective of the most recent results concerning the detection efficiency, temporal jitter and maximum achievable count rate measured on a detector module with a maximum gain of 150. These results have also been used to estimate the performance of this detector as a receiver for long-distance datacom employing Pulse-Position Modulation (PPM) and On-Off Keying (OOK) modulation formats.

The manuscript is divided as follows. In Section 2 the device architecture is described, and details on the basic blocks composing the detector module are given. Section 3 illustrates the experimental setup and the results of basic characterization of the module at unity gain and in linear-mode operation at high gain. In Section 4, the method that was used to reconstruct the meso-photon states obtained by the analysis of the acquired data is presented, and the detector parameters extracted from such measurements are discussed. The assessment of the detector performance for PPM and OOK modulation formats are presented and discussed in Sections 5 and 6, respectively. Section 7 finally presents the conclusions of this work and the future perspectives of HgCdTe APDs for close-to-quantum limited optical communications.

2. DETECTOR ARCHITECTURE

The structure of the detector is schematically presented in Fig. 1. The detection module is based on n/p HgCdTe avalanche photodiodes (APDs) grown on a CdZnTe substrate by liquid phase epitaxy (LPE) and disposed in a four-quadrants configuration with a pitch of $d_{pitch} = 200 \mu\text{m}$ (see Fig. 1a). The HgCdTe APDs consist in a non-depleted mercury vacancy (VHg)-doped p-type region facing the incoming optical signal, in a backside-illuminated architecture.

The photo-generated carriers, which result from the absorption of the incoming photons occurring in the p-side, are amplified and collected by a multiplication layer that is formed by the annealing of the mercury vacancies in a region with residual n-type doping. The corresponding region determines the diameter of the APD (as shown in Fig. 1b). The APD diameter in the detector module that was used to obtain the presently reported data is $\Phi_{APD} = 6 \mu\text{m}$.

In the present case, the HgCdTe epitaxial layer grown on the CdZnTe substrate has a graded band gap that extends over a thickness of ~ 1 to $2 \mu\text{m}$, and a region of constant band gap with a cut-off wavelength of $\lambda_c = 2.9 \mu\text{m}$ at the nominal operating temperature of 80 K. The thin absorbing layer with graded band gap is suitable to detect photons with wavelength ranging between 1 to $2 \mu\text{m}$. The multiplication layer, which extends to the graded band-gap region, has been designed to optimize the collection time and reduce the jitter associated to the multiplication and collection of the carriers generated by the absorption of the incoming photons. In the case of the present design, the jitter of the carriers generated within the APD diameter is expected to be lower than 100 ps. A ZnS-based anti-reflection (AR) coating is finally deposited on the backside-illuminated surface to minimize the reflection of the incident light at the air/CdZnTe interface.

The APD chip is then flip-chip hybridized onto an in-house designed silicon-based CMOS readout integrated circuit (Si-ROIC) by means of indium bumps. The Si-ROIC circuit is based on a high-gain resistive trans-impedance amplifier (RTIA) input stage, which converts the photo-generated current I_{ph} into a voltage signal V_{out} (as schematically shown by Fig. 1c). To improve the rejection of external interferences at the output, the ROIC provides two balanced differential signals per APD. The low impedance connection provided by the flip-chip bonding of the APD chip onto the ROIC circuit ensures a low noise level and a high bandwidth in order to reach the single photon level at high detection rates. The Si-ROIC has been designed to reach a bandwidth of 290 MHz and a low input referred noise of $n_e = 30$ electrons rms.

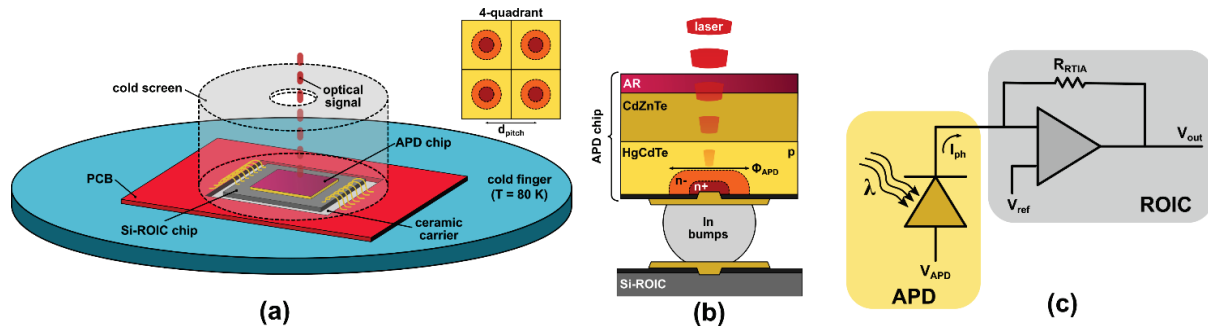


Fig. 1. Architecture of the detector: (a) schematic view of the detection module mounted in the liquid nitrogen-cooled cryostat (in inset: APD disposed in a four-quadrants configuration with pitch of $200\ \mu\text{m}$), (b) cross-section of the HgCdTe APD chip hybridized onto the Si-CMOS ROIC and (c) equivalent electrical circuit of the detector.

To reduce the dark current-induced events and the photonic glow coming from the ROIC and the surrounding environment when operating in the photon-counting regime, the detector requires to be cooled down at a low temperature. For this aim, a liquid nitrogen (LN_2) cooled cryostat has been specifically designed to host the module at a nominal temperature of $T = 80\ \text{K}$, and allowed an autonomous operation of several hours. In order to minimize its thermal impedance, the hybridized chip is directly mounted on the cryostat's cold finger thanks to a highly conductive and low-thermal expansion ceramic carrier and a double-face thermal tape. The cryostat is closed with a quartz window with a C-band AR coating. The background photonic glow of the cryostat chamber and the residual flux coming from the external environment (which is not filtered out by the quartz window) is partially limited by shielding the detector with a metallic cold screen with a field of view of $\text{FOV} = 14^\circ$. A cold filter, which enables to further shield from the environmental light, was not used during the measurements.

The whole chip is then wire-bonded to a filtered buffer amplifier printed circuit board (PCB) designed to accommodate the chip in an aperture at its center (see Fig. 1a), which is used to bias the ROIC and the APD chips and to route the output signals.

3. BASIC CHARACTERIZATION OF THE DETECTOR

3.1 Description of the experimental setup

The module has been characterized using the experimental setup depicted in Fig. 2. A gain switched laser source (Calmar Optcom) emitting at $\lambda_{\text{laser}} = 1550\ \text{nm}$ has been used to generate laser pulses with a pulse width of $\sim 40\ \text{ps}$ and at a repetition rate f_{rate} whose value could be set in a range between $1\ \text{MHz}$ and $1\ \text{GHz}$ ($f_{\text{rate}} = 4\ \text{MHz}$ was set during the measurements, if not otherwise specified). The laser output was then coupled on a single-mode fiber (SMF-28). The jitter of the laser pulses is negligible compared to that of the detector and equal to $\sim 1\ \text{ps}$ (as declared by the laser supplier). The average power of the optical signal sent to the detector was controlled by means of a variable optical attenuator (VOA), which allowed a real-time monitoring of the input power thanks to an integrated power meter. A cascade of three $10\ \text{dB}$ fixed optical attenuators ($30\ \text{dB}$ of attenuation in total) was added after the VOA, in order to reach the single photon level before sending the light on the detector surface.

The setup has been calibrated using a high sensitive optical power meter (ANDO AQ2140) at the end of the fiber. This allowed estimating the optical losses due to fiber connectors and fixed attenuators to be equal to $1.02\ \text{dB}$, which were taken into account to calculate the exact average number μ_{ph} of photons per pulse of the Poissonian light incident on the detector.

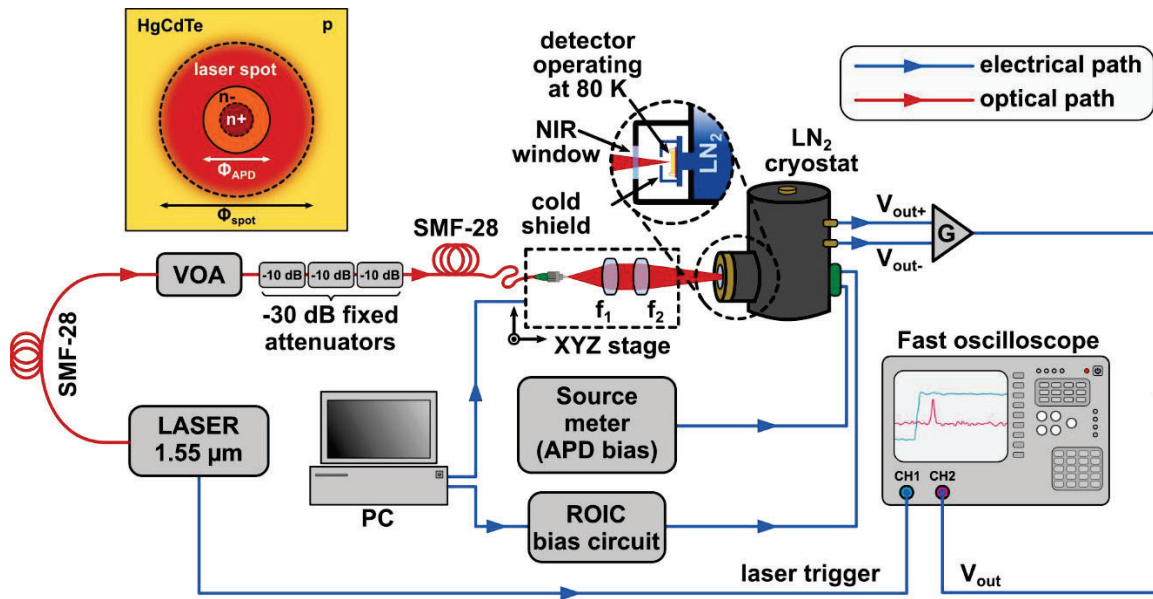


Fig. 2. Experimental setup used during the characterization of the detector. In inset, a schematic comparison between the sizes of the laser spot and the APD is shown ($\Phi_{spot} = 14 \mu\text{m}$, $\Phi_{APD} = 6 \mu\text{m}$).

The optical signal is then focused on the detector using a 2-lens optical system composed by a collimator with focal length $f_1 = 37 \text{ mm}$ and an achromatic lens with $f_2 = 50 \text{ mm}$, which produces a laser spot of $\Phi_{spot} = 14 \mu\text{m}$ in diameter at its waist. This is the smallest achievable laser spot within the current setup. During the calibration, it has been verified that the laser spot was properly focused on the detector through the $\text{FOV} = 14^\circ$ cold screen without any vignetting effect.

Given the smaller dimension of the APDs ($\Phi_{APD} = 6 \mu\text{m}$) with respect the laser spot, the optimization of the optical coupling on the APD surface is critical. To this aim, the alignment and focusing of the laser spot on the APDs is performed thanks to a motorized XYZ positioning stage with micrometric resolution controlled by a PC with an in-house developed software. The PC has been also used to bias the ROIC circuit by means of the filtered buffer amplifier PCB board, while a source meter (Keithley 236) was employed to bias the APDs and measure the average current generated by the APDs. The average photocurrent I_{ph} induced by the absorption of the laser pulses has been obtained by measuring the variation $I_{ph} = I_{on} - I_{off}$ between the average current when the laser was turned on (I_{on}), and the background current of the APDs when the laser was switched off (I_{off}). It is worth mention that, while I_{off} is related to the background current generated by the four APDs conjointly, I_{on} can be essentially attributed to one APD only, because of the large inter-pixel spacing between the APDs forming the four-quadrants detector ($d_{pitch} = 200 \mu\text{m}$) and the relatively small dimensions of the laser spot ($\Phi_{spot} = 14 \mu\text{m}$). The two differential outputs provided by one APD were converted into a single-ended signal V_{out} by means of a differential amplifier (Maxim MAX 4444) with a gain $G = 2$, prior to its acquisition by a fast real-time sampling digital oscilloscope (Teledyne Lecroy WavePro 725Zi) with 8-bit resolution, 2.5 GHz bandwidth and sampling rate up to 40 GS/s. A digital pre-processing filter with a cut-off frequency of 580 MHz was also applied during the acquisition of data.

3.2 Characterization of the detector module at unity gain ($M = 1$)

The experimental setup described above has been used to characterize the detector at unity APD gain. From the analysis of the pulse response at low APD bias acquired by the oscilloscope, it is possible to determine the performance of the APD and ROIC chips. The average value of these, which are summarized in Table 1, have been obtained by averaging the data over 2500 acquisitions.

When the laser spot is well focused on one of the APDs composing the four-quadrants, the impulse response of the detector is mainly limited by the bandwidth of the RTIA amplifier. An example of a single pulse response at unity gain recorded by the real-time oscilloscope is presented in Fig. 3. In this case, the response was obtained at an APD bias of $V_{APD} = -0.5 \text{ V}$ for an average incident power of $P_{inc} = -65.06 \text{ dBm}$ (311.9 pW), corresponding to $\mu_{ph} = 608$ photons/pulse in average at

a frequency rate of $f_{rate} = 4$ MHz. Attention has been paid to set the value of the incident optical power such as the detector response was not saturated.

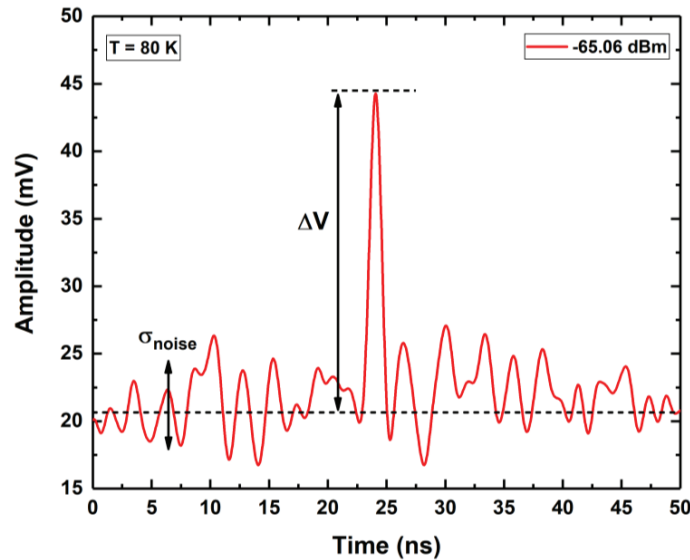


Fig. 3. Impulse response of the APD detector at unity gain ($V_{APD} = -0.5$ V) and $T = 80$ K for an average incident power of $P_{inc} = -65.06$ dBm, corresponding to $\mu_{ph} = 608$ photons/pulse at $f_{rate} = 4$ MHz.

In such conditions, an average amplitude of about 27.8 mV was measured, with a rise time and a fall time equal to $\tau_{rise} = 780$ ps and $\tau_{fall} = 730$ ps, respectively. The slower (i.e. τ_{rise}) has been considered to calculate the detector bandwidth, which is estimated to $BW_d = 450$ MHz, which it turns to be higher than the designed one (290 MHz). The width of the pulse response was equal to $FWHM = 1173$ ps. These results can be compared with measurements on a similar APD hybridized onto an interconnection network and measured with a small optical spot diameter of ~ 5 μm and a low gain broadband RF amplifier with a 25 GHz-bandwidth, for which the rise time and fall time were ~ 45 ps and 190 ps, respectively. These results show that the temporal resolution of the detector is presently limited by the ROIC bandwidth. Further improvements of the detector bandwidth can be achieved by increasing the Si-ROIC bandwidth, provided that the optical coupling of the light within the APD area is optimized to avoid a slow diffusion-limited detected signal.

Table 1. Detector average parameters obtained from the pulse response measurements at unity gain ($V_{APD} = -0.5$ V).

Parameter	Description / Formula	Value
P_{inc} (dBm)	average incident optical power	-65.06
P_{inc} (pW)		311.9
f_{rate} (MHz)	pulsed laser frequency rate	4
V_{APD} (V)	APD (reverse) bias voltage	-0.5 V
ΔV (mV)	pulse amplitude	27.81
M (adimensional)	APD multiplication gain	1.02
σ_{noise} (mV)	noise standard deviation	2.74
I_{off} (nA)	background APD current (laser off)	0.01
I_{on} (nA)	laser-induced current (laser on)	0.30
I_{ph} (nA)	photo-generated current	0.29
τ_{rise} (ps)	pulse response rise time (10% to 90%)	780

τ_{fall} (ps)	pulse response fall time (90% to 10%)	730
$FWHM$ (ps)	pulse width (full width at half maximum)	1170
BW_d (MHz)	detector bandwidth $BW_d = \frac{0.35}{\tau_{rise}}$	450
μ_{ph} (photons/pulse)	average number of photons per pulse $\mu_{ph} = \frac{P_{inc}}{f_{rate} \times \frac{hc}{\lambda_{laser}}}$	608
N_e (electrons/pulse)	average number of photo-generated electrons per pulse $N_e = \frac{I_{ph}}{q \times f_{rate}}$	453
G_{RTIA} (k Ω)	trans-impedance gain $G_{RTIA} = \frac{\Delta V}{N_e \times \frac{q}{2 BW_d}}$	426
G_{ROIC} (mV/electrons)	voltage-electron conversion gain $G_{ROIC} = \frac{\Delta V}{M \times N_e}$	0.061
n_e (electrons rms)	ROIC input referred noise $n_e = \frac{\sigma_{noise}}{G_{ROIC}}$	45
EQE (%)	detector external quantum efficiency $EQE = 100 \frac{N_e}{M \times \mu_{ph}}$	73

$$q = 1.602 \times 10^{-19} \text{ C is the electric charge}$$

$$h = 6.626 \times 10^{-34} \text{ J s is the Planck constant}$$

$$c = 3 \times 10^8 \text{ m/s is the speed of light (in vacuum)}$$

The output noise at $V_{APD} = -0.5 \text{ V}$ was equal to $\sigma_{noise} = 2.74 \text{ mV}$, which corresponds to an input referred noise of 45 electrons rms. This is higher than the expected value obtained by simulations during the design of the ROIC circuit, and it can be explained by the higher bandwidth of the RTIA amplifier and by the presence of poles near the cut-off frequency of the frequency response of the detector, which increase the noise.

As previously discussed, due to the small dimension of the APD surface with respect to the laser spot area, the optical coupling offered by the current experimental setup can set a limit of the maximum achievable quantum efficiency. In the present detector, the measured quantum efficiency is indeed limited to a value of $EQE = 73\%$. This value is also affected by the response of the AR coating layer. Indeed, the thickness of the AR layer did turn out to differ from the nominal value, resulting in a maximum transmission at 2175 nm (instead of 1550 nm) and thus decreasing the EQE at the laser wavelength. The EQE can thus be improved by choosing a 1550 nm-matched AR coating to maximize the detector responsivity at this specific wavelength, by enhancing the optical coupling with integrated micro-lenses realized on the surface of the detector to further focus the light within the APD area and by using new APDs with larger area. These solutions are currently under development and it will be soon tested.

3.3 Characterization of the HgCdTe APD-based detector for linear-mode photon-counting operation

The multiplication gain M offered by the present detector is plotted in Fig. 4a. For an APD bias voltage $V_{APD} \leq -15.5 \text{ V}$, a value exceeding 100 was obtained, with a maximum value of $M = 155$ obtained at -16.5 V . At this value of the APD bias voltage (-16.5 V), the APD tunneling current start slightly appearing, increasing the dark current and spoiling the noise performance of the detector. In the same plot, the measured input referred noise of the ROIC circuit (and its expected value, for comparison) is indicated. In order to properly detect optical signals at the single photon level with a high signal-to-noise ratio (SNR), a gain at least twofold higher with respect to the ROIC input referred noise is preferred (i.e. $M \sim 90$).

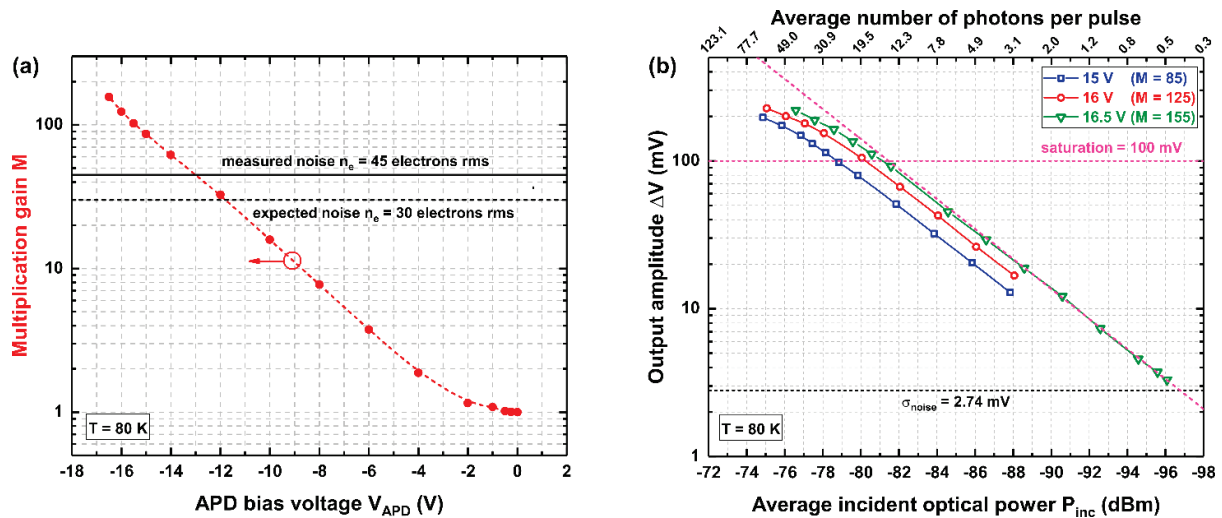


Fig. 4. (a) APD multiplication gain as a function of the APD bias voltage. The expected and the measured ROIC input referred noise are indicated for comparison (dashed and solid black lines, respectively). (b) (Average) output voltage characteristic as a function of the average incident optical power for three different APD bias (blue squares: -15 V, red circles: -16 V, green triangles: -16.5 V). The dashed pink line is a linear fit on the -16.5 V curve. The average number of photons per pulse is also indicated (pulsed laser frequency rate $f_{rate} = 4$ MHz).

In Fig. 4b the average output voltage characteristics of the detector as a function of the incident optical power (and the average number of incident photons μ_{ph}) is shown, for three different APDs bias voltages corresponding to multiplication gains between 85 and 155. The deviation of the output characteristic from a linear behavior can be highlighted by plotting the linear fit obtained from the points with an amplitude < 20 mV (dashed pink line). A -10% drop from the linear fit is reached for output amplitudes close to 100 mV, although a slight deviation from linearity can be observed starting from values around 45 mV. This gives a linear dynamic range of 10 dB, enabling linearly detection of photons with some margin in the range 1 to 12 photons/pulse at -16.5 V. It is worth mentioning that the dynamic range of detection can be extended while still preserving a linear behavior by changing the bias voltage of the APD during operation, so that mesoscopic photonic states of several tens of photons per pulse can in principle be detected.

For the present module, a total background current of 0.59 nA for the four APDs has been measured for an APD bias voltage of -15V. Supposing that the current is fully amplified by the four APDs, this corresponds to an unamplified background current of 1.2 pA per APD. This is higher than the expected IR current for a device with a 300 K cut-off wavelength of $\lambda_c = 3 \mu\text{m}$ (which is equal to 0.5 pA), and it can be related to the glow of the ROIC circuit, or an unexpected higher dark current of one APD. We highlight that in the present detector, no metallic blocking layer was employed to shield the APDs from the glow of the ROIC circuit, which is just underneath the APDs. Also, the unamplified background current per APD increases to 2.5 pA at -16.5 V, which is probably induced by the appearance of the tunneling current of the APDs, as discussed above.

An example of acquisition performed at a single photon level with an APD bias of -15 V is presented in Fig. 5. In such a regime, the noise is still dominated by the ROIC contribution and is equal to 2.76 mV (value of the noise standard deviation). On the left (Fig. 5a) is shown a set of six waveforms acquired when the laser is switched off. From time to time, the generation of carriers due to the absorption of infrared photons related to the incident residual flux on the detector or the glow of the ROIC circuit, together with the amplification of carriers related to the dark current of the APD, can eventually trigger a multiplication process resulting in a ‘dark count’ event. The black arrows of Fig. 5a indicate these events, which appears randomly in time. When the laser is turned on, pulses are detected around the expected instant of detection t_0 (which in this case is $t_0 = 20$ ns, dashed black line on Fig. 5b). The signals shown in Fig. 5b have been obtained for a Poissonian photon state with $\mu_{ph} = 1.5$ photons/pulse. The variable amplitude of the detected pulses, or their absence (see sample #4 in green, Fig. 5b), reflects the discreteness nature of the detection process. This is due to the absorption of a variable number of photon per pulse due to the Poissonian nature of the incident light, together with the fluctuation in the multiplication gain of the APD (which corresponds to an excess noise factor $F > 1$).

In the next section, we discuss the procedure that has been developed to post-process such data acquired with the oscilloscope, and to extract the information that is contained in the waveforms composing each dataset.

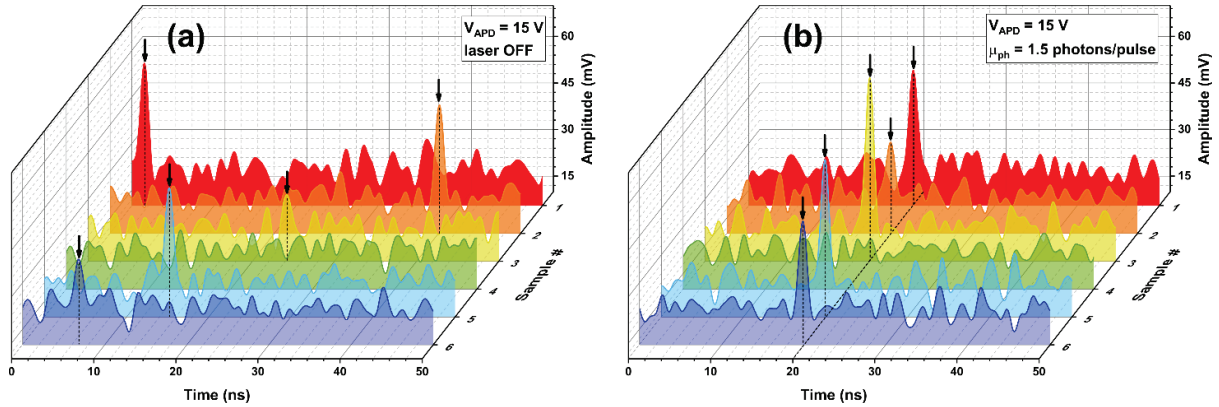


Fig. 5. Example of acquired waveforms at a single photon level: (a) with the laser off (residual flux on the detector) and (b) in the case of an incident photonic state with an average number of photons per pulse equal to $\mu_{ph} = 1.5$. The APD was biased to -15V. A black arrow indicates a detection event.

4. MESO-PHOTONIC STATES DETECTION WITH HgCdTe APD DETECTORS OPERATING IN LINEAR-MODE

4.1 Meso-photonic state reconstruction

In this section, the method that has been developed to post-process the data and reconstruct the histograms of the photonic distributions is presented. It allows extracting the information associated to the detected meso-photonic states. Additionally, the same method allows estimating some key parameters of the detector, such as the detection efficiency η_d and the excess noise factor F . These two last parameters define the QE to F ratio (or $QEFR$), which quantify the conservation of the information contained in a shot-noise limited photonic signal in linearly amplified photo-detectors. For a given average incident optical power P_{inc} (i.e. a given photonic state with an average number μ_{ph} of photons per pulse), a dataset composed of 10k waveforms was acquired. Each waveform of a specific dataset is then fitted with a non-linear least-square minimization procedure implemented in Python. This procedure allows fitting the real-time waveforms by a Gaussian function defined as follows:

$$y = y_0 + A_p e^{-\frac{(t-t_c)^2}{2\sigma_c^2}} \quad (1)$$

where:

- t is the time;
- y_0 is the baseline value, which has been set equal to a value around 22.0 mV, eventually allowing it varying in a ± 0.5 mV interval around that value to adjust the fit;
- t_c is the peak position of the detected pulse (i.e. the instant of detection of the pulse), it can vary in a window width of $\Delta t = \pm 6$ ns around the expected average arrival time t_0 , which is used as an initial guess to help the fitting procedure reaching the convergence;
- σ_c is the standard deviation of the pulse, which is related to the full width at half maximum ($FWHM$) of the peak according to $FWHM = 2 \sqrt{2 \ln(2)} \sigma_c \approx 2.35 \sigma_c$. The $FWHM$ has been set equal to 1.1 ns and it has been kept fixed during the procedure. This value has been chosen by measuring the width on single detection events, and its value

is reduced with respect to the value measured at unity gain (~ 1.2 ns), which is increased by a non-negligible contribution of the collection time of carriers at low APD bias;

- A_p is the pulse amplitude, with no set boundaries.

We stress the fact that the data were processed by setting the $FWHM$ to a fixed value and let the others parameters to be adjusted in a selected range in order to get the best fit to the acquired single photon pulses and obtain information about the amplitude A_p and time of detection t_c . Details on the fitting procedure can be found in [10].

This procedure was applied to datasets with a large number N_{tot} of waveforms ($N_{tot} = 10000$), which have been acquired at different values of the calibrated average incident power P_{inc} , each dataset corresponding to a different Poisson photonic states with average photon number equal to μ_{ph} .

Fig. 6 shows the outcomes from the fitting of three waveform samples, recorded with an average incident optical power of $P_{inc} = -92.96$ dBm (corresponding to an average number of photons/pulse equal to $\mu_{ph} = 1$) and a detector bias of $V_{APD} = -15$ V. The figure shows the cases of:

- a fit on a detection event (Fig. 6a);
- a fit on the electronic noise when no photons is absorbed, or the photo-generated carriers are not sufficiently multiplied by the avalanche gain. In this case, the algorithm may indistinctly fit on the noise with a positive (Fig. 6b) or a negative amplitude (Fig. 6c).

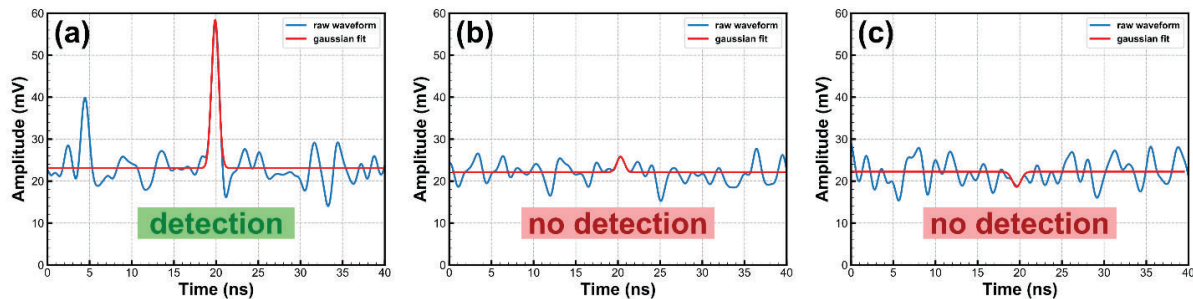


Fig. 6. Examples of three possible outcomes of the fitting procedure on experimental waveforms, in the case of $P_{inc} = -92.96$ dBm (at $f_{rate} = 4$ MHz), corresponding to $\mu_{ph} = 1$ photons/pulse in average, and $V_{APD} = -15.5$ V. Fitting on: (a) a detection event, and (b,c) electronic noise with positive or negative amplitude, respectively.

The procedure allows reconstructing the histograms of the pulse amplitudes for different datasets related to a specific photonic state characterized by an average number of incident photons per pulse μ_{ph} . The raw histograms can be translated into the photo-electron probability distributions and fitted with a model based on Poisson statistics, which takes into account the APD and ROIC responses, characterized by the mean multiplication gain M of the APD, the detection efficiency η_d , the excess noise factor F and the ROIC voltage-electron conversion gain G_{ROIC} and noise σ_{noise} . Fig. 7 shows the result of such a procedure in the case of three meso-photonic states characterized by an average photon number μ_{ph} equal to 7.5, 15 and 25, respectively.

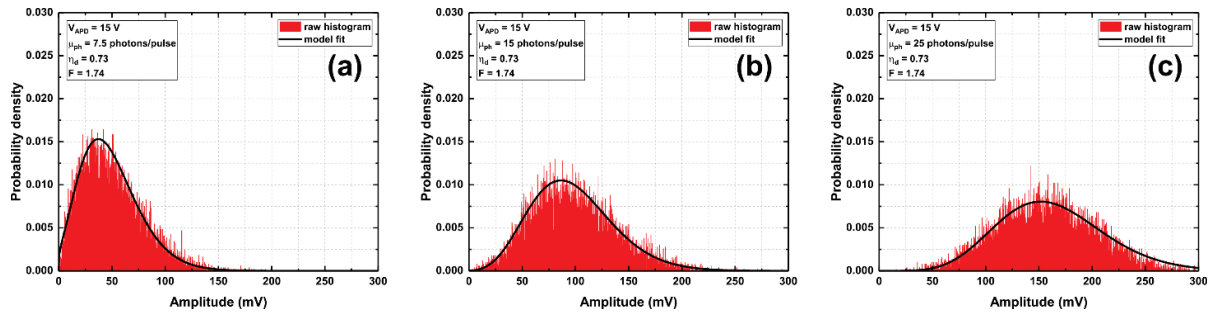


Fig. 7. Red bars: output amplitude histograms obtained by the post processing fitting procedure in the case of an average incident number of photons per pulse equal to (a) $\mu_{ph} = 7.5$, (b) $\mu_{ph} = 15$ and (c) $\mu_{ph} = 25$ (at $f_{rate} = 4$ MHz, $V_{APD} = -15$ V). Black solid line: photonic state model fit obtained with a detection efficiency $\eta_d = 0.73$ and an excess noise factor $F = 1.74$, for an average number of incident photons per pulse equal to 7.5, 15 and 25, respectively.

4.2 Detection efficiency, excess noise factor and QEFR estimation

The analysis of the photo-electron probability distributions allowed estimating a detection efficiency of $\eta_d = 0.73$, in agreement with the value of EQE estimated at unity gain, and an excess noise factor $F = 1.74$, that is above the expected value for HgCdTe APDs. The parameters corresponding to the best fitting of the amplitude distributions are summarized in Table 2. From the detection efficiency and the excess noise, it is possible to calculate the $QEFR = \frac{QE}{F}$, which gives an estimation about how much the information contained on the detected signals is preserved.

Table 2. Parameters extracted from the analysis of the photo-electron probability distributions.

Parameter	Value
η_d	0.73
F	1.74
$QEFR$	0.42

We highlight the fact that the excess noise factor that has been observed in the present detector is relatively higher than previously reported values in literature (typical values for SWIR HgCdTe APDs ranging from $F = 1.1$ to 1.4) [10-13], while the $QEFR$ is typically higher than 0.50 for different HgCdTe cut-off wavelengths λ_c . We believe that the degradation of the excess noise factor (and the $QEFR$) observed on the present detector is most likely due to an inhomogeneity of the gain response across the APD surface. Such behaviour have been evidenced in several APDs coming from the same batch as the present APDs, using a dedicated optical bench that allowed focusing a smaller optical spot within the diameter of the APDs. These measurements evidenced a strong reduction of the multiplication gain at the center of the diodes with respect to their sides. Such spatial variation of the gain leads to an extrinsic contribution to the excess noise factor. It is also possible that in the present APDs a non-negligible absorption of the incident optical flux takes place on the multiplication layer, which has the effect of increasing the excess noise.

The degradation of the excess noise factor has an impact on the $QEFR$, which in the present device is lower than expected. An optimized APD technology with capability to form larger area APDs and a more homogeneous multiplication layer with high gain, lower excess noise and faster response (reduced jitter) is currently under development at CEA-Leti and it is expected to solve the current limitations.

5. DETECTOR PERFORMANCE FOR PULSE-POSITION MODULATION OPTICAL COMMUNICATIONS

The four-quadrants detector module described in the previous sections has been designed to serve as a ground receiver for deep-space optical links, detecting $1.55 \mu\text{m}$ data streams from satellites. In the framework of the collaboration with the European Space Agency, we were interested in assessing the performance of our detector for Pulse-Position Modulation

(PPM) format for the Deep-space Optical Communication System (DOCS), which is currently in preparation for future ESA space missions [14,15]. In this modulation format, the information is encoded in the temporal position of the pulse and beside the detection efficiency, another key parameter is the temporal jitter of the detected pulses that can introduce temporal bin errors.

ESA's requirements for the PPM communication performance set a maximum value for the false alarm probability equal to 10^{-2} (with a preferred goal of 10^{-3}), a minimum detection probability of a pulse in the correct temporal bin equal to 0.9 (preferred: 0.99), a minimum PPM slot width of 500 ps and a minimum signal per pulse equal to 5 photons.

To assess the performance of our detector for such an application, the procedure described in Section 4 was applied to reconstruct the histograms of meso-photon states with an average photon number μ_{ph} equal to 5 and 10 photons/pulse at an APD bias voltage of -15.5 V ($M=102$), as well as for the "OFF" state (corresponding to the residual photon flux incident on the detector). From the histograms of the distributions, the cumulative distribution function (CDF) related to the two photonic states, and the complementary cumulative distribution function (CCDF = 1 - CDF) for the "OFF" state were calculated, as shown in Fig. 8a.

From the CDFs the detection probability (which includes the zero-photon Poisson probability) is obtained. Similarly, the false alarm probability can be obtained from the CCDF of the "OFF" state.

It can be seen that for $\mu_{ph} = 5$ photons/pulse the specifications cannot be met, since the threshold voltage to reach a detection probability of 0.9 corresponds to a false alarm rate above 10^{-2} . In the case of the photonic state with $\mu_{ph} = 10$ photons/pulse, the specifications on the detection probability of 0.99 and the false alarm probability of 10^{-2} are reached simultaneously (intersection of the two curves, indicated by the cyan dashed curve on Fig. 8a). Accepting a penalty in the detection probability of 0.9, the rejection of the false pulses can be improved (false alarm probability equal to 1.2×10^{-3} , orange dashed line). We stress the fact that a strong improvement in the performance is expected using optimized APDs with homogeneous gain and corresponding higher QEFR that are currently under development, which may result in a specification compliance for a photonic flux with an average photon number below 5 photons/pulse. Also, the false alarm probability measured in the present detector is limited by the high amplitude spurious dark counts (DC) tail of the CCDF, as it can be observed in the figure. As in the present detector no cold filter was implemented, the false alarm probability is expected to be further improved by suppressing a part of these dark counts events. A further improvement is expected from an effective blocking of the ROIC glow.

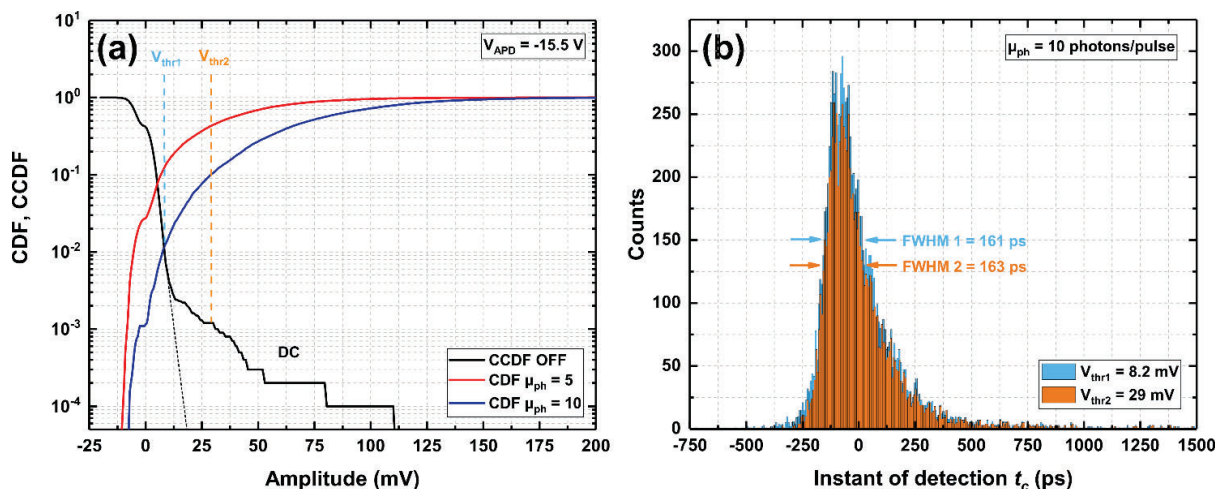


Fig. 8. Detector performance evaluation for PPM format: (a) Cumulative distribution function (CDF) for a photonic state with an average incident number of photons equal to $\mu_{ph} = 5$ (solid red line) and $\mu_{ph} = 10$ photons/pulse (solid blue line) compared to the complementary cumulative distribution function (CCDF) of the "OFF" state (residual flux). The colored dashed lines indicate the threshold points at which the CDF_{10ph} reaches 10^{-1} (cyan dashed line, $V_{thr1} = 8.2$ mV) and 10^{-2} (orange dashed line, $V_{thr2} = 29$ mV), respectively. The black dotted line is a linear extrapolation on the "OFF" state CCDF to highlight the contribution of the dark counts (DC) to the false alarm rate. (b) Distribution of the instant of detection of pulses with amplitudes exceeding $V_{thr1} = 8.2$ mV (cyan) and $V_{thr2} = 29$ mV (orange), in the case of $\mu_{ph} = 10$ photons/pulse.

The detection probability within a slot width of 500 ps is 0.9 and do comply with ESA's specification. The temporal jitter of the detected response was also estimated, as presented in Fig. 8b. To do that, the distribution of the instant of detection t_c of pulses was reconstructed by setting a threshold for the pulse amplitude equal to $V_{thr1} = 8.2$ mV (cyan histogram) and $V_{thr2} = 29$ mV (orange histogram), corresponding to the two intersection points discussed above, for which the specification on detection probability and false alarm probability are met. From the histograms, the FWHM of the distributions was extracted. In both cases, the temporal jitter distribution was characterized by a FWHM around 160 ps. It is worth to mention that this value is affected by the contribution of diffusion-limited detected events, because in the actual setup the laser spot diameter ($\Phi_{spot} = 14 \mu\text{m}$) is more than twofold the size of the APDs ($\Phi_{APD} = 6 \mu\text{m}$), thus the photons that are absorbed outside the APD area strongly contribute to the increase of the temporal jitter. The implementation of a micro-lenses array together with the use of a larger area APDs would dramatically improve the optical coupling of the optical signal within the APDs area, with the double benefit of reducing the temporal jitter of the detected response and increasing the detection efficiency. Both these approaches are currently under development.

6. DETECTOR PERFORMANCE FOR OOK MODULATION OPTICAL COMMUNICATIONS

In this section the results from the characterization of the device to estimate the expected performance when used as a receiver in a 625 Mbps free-space optical link are discussed. The detector was tested using the experimental setup shown in Fig. 9a.

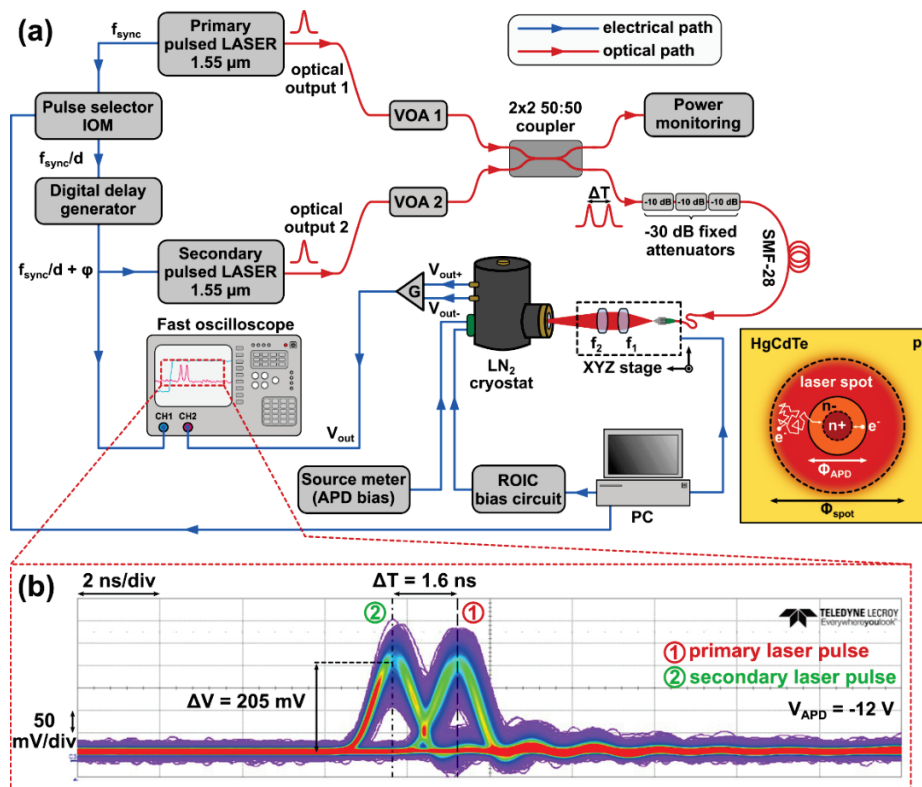


Fig. 9. Free-space datacom evaluation test-bench: (a) experimental setup used to generate two synchronous optical pulses with a controllable variable delay ΔT . (b) Example of acquired signal for an APD bias of -12 V and an incident optical power equal to 96 and 86 photons/pulse for the primary and secondary pulse, respectively. The inset schematically shows the effect of the actual optical coupling on the photo-generation of carriers inside or outside the APD area: the collection of the former is rapid, while the collection of the latter is limited by diffusion.

In this setup, two separated 1.55 μm -emitting pulsed laser modules (indicated as “primary” and “secondary” in the following) were used to generate consecutive optical pulses. The primary laser (Mendocino Fiber Laser, Calmar Laser) generates pulses with a <0.5 ps width and a negligible time jitter (< 100 fs), at a fixed repetition rate $f_{rate1} = 10$ MHz. The trigger output voltage of the primary laser has been used to synchronize the emission of the secondary laser. To do that, a pulse selector (IOM, LaCoSys IOM-150) with a division factor $d = 10$ has been used to generate a TTL voltage signal at a frequency rate $f_{rate1}/d = 1$ MHz. This signal has been sent to a digital delay generator (DG535, Stanford Research Systems), able to introduce an arbitrary delay ΔT (adjustable with a 5 ps resolution) to the TTL voltage signal. In such a way, secondary laser pulses with a controllable delay set to $\Delta T = 1.6$ ns (corresponding to a frequency difference of $\Delta f = 625$ MHz) were generated. The optical output of both lasers was coupled to a single mode SMF-28 optical fiber as shown in the Fig. 9a. The jitter contribution of the pulse selector and the digital delay generator to the optical output produced by the secondary laser was measured with a commercial fast InGaAs photodiode (with 10 GHz bandwidth) to have an rms value equal to 85 ps.

Two separated VOAs were employed to independently adjust and balance the average incident power of each arm. The two optical outputs were recombined by using a bidirectional 2×2 ports 50:50 optical coupler. One output port of the 50:50 coupler was employed to constantly monitor the average optical power sent to the detector (with the high sensitive fibered optical power meter), while the other output port was used to couple the light on the detector. A cascade of three 10 dB fixed optical attenuators was added to that port. The optical signal was then focused on the detector by using the same 2-lens system previously described in Section 3, producing a laser spot of 14 μm in diameter. The optical power meter were used to precisely calibrate the optical losses on both optical paths, in order to estimate the exact amount of incident optical power that was incident on the detector, prior to its characterization. The single-ended output V_{out} of the detector has been then acquired with the real-time sampling oscilloscope. Fig. 9b shows an example of acquired waveforms obtained by using the previously described setup, for an APD bias of -12V and an average incident number of photons per pulse equal to 96 and 86 for the primary and the secondary laser pulse, respectively. It can be seen that the two detected pulses are clearly separated and distinguishable. However, the tail of the secondary pulse (indicated by 2 in Fig. 9b) results in a degradation of the signal-to-noise ratio of the primary pulse (indicated by 1 in Fig. 9b), which can be noted by observing the ‘eye’ generated by the two pulses, the former being more open than the latter. The origin of the tail of the acquired optical signals is mainly due to the fluctuation of the instant of detection of the photons, combined with the oscillation of the signal after each impulse and, to a lesser extent, of the ROIC noise. The former is a consequence of the optical coupling on the diode, as schematized in the inset of Fig. 9a. As discussed above, as the laser spot is bigger than the diode area ($\Phi_{spot} = 14 \mu\text{m}$ vs $\Phi_{APD} = 6 \mu\text{m}$), the carriers that are photo-generated outside the APD area will be collected by diffusion and thus contribute to a slow and fluctuating collection time, responsible for the tail in the timing jitter of the detector at low photon number signals. Again, the use of larger area APDs and micro-lenses to improve the optical coupling would be beneficial to improve the timing jitter and to suppress the tail of the detector response.

This experimental set-up was used for characterization of the detector module with the goal of estimating its performance if used in a simple On-Off Keying (OOK) modulation scheme. To present, the analysis was limited to the first incoming pulse (the secondary laser pulse of Fig. 9b). This analysis neglects the noisy response tail and gives thus the best-case scenario that can be achieved with the present detector associated to an optimal optical coupling.

To estimate the detector performance in a 625 Mbps OOK modulation operation, the procedure described in Section 4 was applied. The histograms of the meso-photon states were estimated for an average photon number μ_{ph} ranging from 7.5 to 25 photons per pulse, as well as for “OFF” states when the laser was switched off (i.e. the residual flux). The amplitude distribution for the “OFF” state were also estimated from measurement in dark conditions, i.e. when the residual flux was screened by a closed cold screen ($\text{FOV} = 0^\circ$) placed in front of the detector module, in order to compare with the situation in which a cold filter would be implemented.

For this analysis, the incident instant of detection t_c was fixed and equal to the expected pulse arrival time t_0 . The processing of the data allowed reconstructing the CDF for the meso-photon states and the CCDF for the “OFF” state with and without residual flux. The results of such measurements are summarized in Fig. 10a. The bit-error rate (BER) expected for a 625 Mbps OOK can be estimated from the interception points between the meso-photon CDF curves and the CCDF curve with and without residual flux. The interception points for the $\mu_{ph} = 20$ and $\mu_{ph} = 25$ photons/pulse curves with the CCDF curve without residual flux have been estimated from an extrapolation of the CDF curves. The results are presented in Fig. 10b, where the calculated BER is plotted as a function of the recalculated equivalent incident optical power P_{eq} . The associated average number of photons per bit N_s , supposing an ideal OOK modulation format with perfect extinction ratio, is given by [16]

$$N_s = \frac{N_{ON} + N_{OFF}}{2} = \frac{N_{ON}}{2} \quad (2)$$

where $N_{ON} = \mu_{ph}$ is the average number of photons for the “ON” (1) bit and $N_{OFF} = 0$ is the average number of photons for the “OFF” (0) bit. The equivalent incident optical power is thus [16]

$$P_{eq} = N_s h\nu B \quad (3)$$

B being the bit rate (in this case, $B = 625$ Mbps) and $h\nu$ the energy of the incident photons (in this case for $\lambda_{laser} = 1550$ nm). In Fig. 10b the calculated BER at the quantum (shot-noise) limit is also indicated, for comparison.

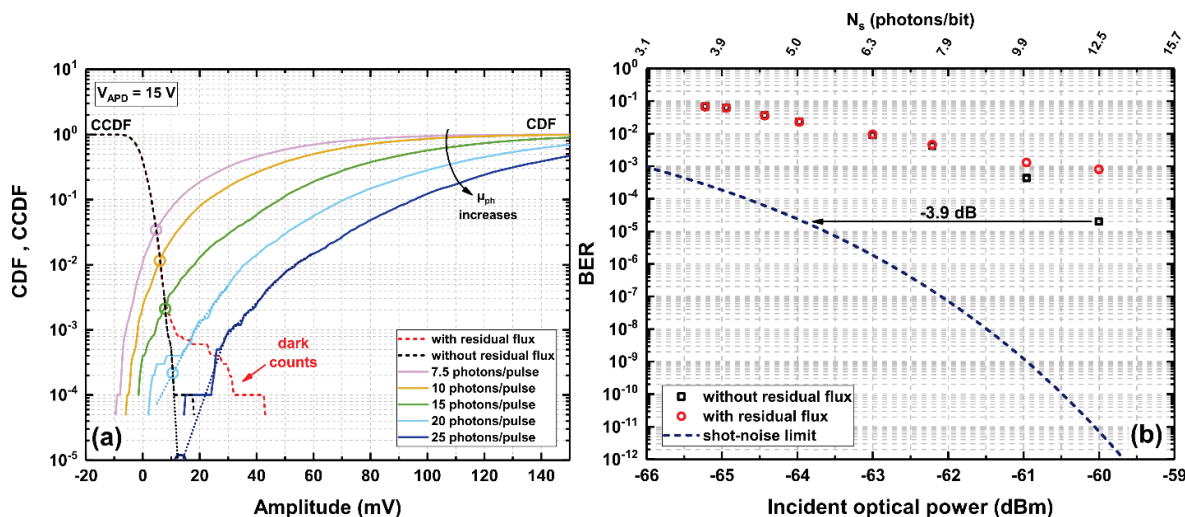


Fig. 10. Performance estimation for a 625 Mbps OOK modulation format. (a) CDF in the case of photonic states ranging from 7.5 to 25 photons per pulse (colored solid lines), and CCDF curves obtained with (dashed red line) and without (dashed black line) the residual flux, for $V_{APD} = -15$ V. Dotted linear extrapolation is shown for the CDF curves with 20 and 25 photons/pulse. Colored circles show the interception points between the CDF and CCDF without residual flux. (b) BER estimation as a function of the equivalent incident optical power (and the equivalent number of photons per bit N_s) with and without residual flux. The shot-noise limited BER is shown for comparison (dashed blue line).

The penalty in sensitivity with the present detector can be estimated from the difference in power between the measured and the quantum limited BER. At $N_s = 12.5$ photons per bit and $BER = 2 \times 10^{-5}$ this penalty is -3.9 dB (black arrow in Fig. 10b). This value, corresponds to ratio in power of 0.41, in good agreement with the value of the $QEFR$ ($QEFR = 0.42$) obtained from the analysis of the meso-photon distributions discussed in Section 4. This result indicates that for high enough signals and/or APD gain, the BER for OOK is directly related to the $QEFR$ of the detector. At lower values of N_s the penalty tends to increase due to the increased contribution from the dark noise of the detector. These observations shows that the penalty can be reduced through increased $QEFR$ and APD gain while minimizing the dark counts and the timing jitter of the APDs. These improvements are expected through present efforts to optimize the APD technology at CEA-Leti.

7. CONCLUSIONS AND PERSPECTIVES

The architecture and characterization of a four-quadrants detection module based on HgCdTe APDs have been presented. The module is designed to be employed as high data rate ground-segment detection module for 1.55 μm deep space optical communications in collaboration with the European Space Agency. The present detector, which is characterized by a multiplication gain in excess of 150, an input referred noise of 45 electrons rms at unity gain and a bandwidth of 450 MHz, enables linear-mode detection of meso-photon states down to the single-photon level at high count rates, approaching 2

GHz if the signal is dispatched on the four quadrants. The characterization of the module evidenced a degradation of the excess noise factor $F = 1.74$ associated with a detection efficiency of $\eta_d = 0.73$ and a temporal jitter of 160 ps (FWHM) at 10 photons per pulse. The high excess noise has been attributed to a non-homogeneous gain response across the APD area, together with an un-optimized optical coupling within the APD area. The latter is also responsible for strong tail in the response time jitter of the detector, due to a highly random diffusion collection of carriers generated outside the area of the multiplication layer.

The detector was used to perform first estimation of the performance for low signal free space optical communication using PPM and OOK modulation formats. Despite the optimizable performance of the present detector module, the results shows that a detection probability of 90% associated with a low false alarm rate can be reached at 10 photons per bit and a time slot width of 500 ps. The estimation of the detector performance for OOK modulation showed that the bit error rate is limited by the information conservation figure of merit of the detector, measured by the quantum efficiency to excess noise ratio ($QEFR$) of the detector, corresponding to a -3.9 dB penalty for 12.5 photons per bit at a BER of 2×10^{-5} .

It is strained that this high performance was achieved with a detector with limited performance in EQE , excess noise and response time jitter. These limitations are currently addressed with the development of a modified APD technology with capability to form larger area APDs with more homogeneous multiplication layer, that is expected to enable higher gain, lower excess noise and faster response (reduced jitter). Also, the use of integrated micro-lenses will allow improving the optical coupling and further increasing the detection efficiency, while simultaneously reducing the temporal jitter of the detected response.

8. ACKNOWLEDGEMENTS

The authors wish to thank Igor Zayer, Sinda Mejri and Clemens Heese from ESA-ESOC for fruitful discussions about the development of the detector module.

9. FUNDINGS

This work was funded by the European Space Agency (ESA contract No. 4000121291/17/D/MB) and by the French LabEx FOCUS (grant ANR-11-LABX-0013).

REFERENCES

- [1] Tosi, A., Acerbi, F., Anti, M., and Zappa, F., "InGaAs/InP Single-Photon Avalanche Diode With Reduced Afterpulsing and Sharp Timing Response With 30 ps Tail," *IEEE J. Quantum Electron.* 48(9), 1227-1232 (2012)
- [2] Holzman, I., and Ivry, Y., "Superconducting Nanowires for Single-Photon Detection: Progress, Challenges, and Opportunities," *Adv. Quantum Technol.* 2, 1800058 (2019)
- [3] Krainak, M. A., Yang, G., Sun, X., Lu, W., Merritt, S., and Beck, J., "Novel photon-counting detectors for free-space communication," *Proc. SPIE* 9739, 97390T (2016)
- [4] Rothman, J., Bleuet, P., Andre, L., Abadie, Q., Bordot, G., Bisotto, S., Audoit, G., Nicolas, J.-A., Dupont, B., Rostand, J.-P., and Lasfargues, G., "HgCdTe APDs for free space optical communications," *Proc. SPIE* 10524, 1052411 (2018)
- [5] Rothman, J., Bleuet, P., Abergel, J., Gout, S., Lasfargues, G., Mathieu, L., Nicolas, J.-A., Rostaing, J.-P., Huet, S., Castelein, P., Aubaret, K., Saint-Pé, O., "HgCdTe APDs detector developments at CEA/Leti for atmospheric lidar and free space optical communications," *Proc. SPIE* 11180, 2018 International Conference on Space Optics (ICSO 2018), 111803S (2019)
- [6] Huntington, A., Compton, M., Coykendall, S., Soli, G., and Williams, G. M., "Linear-mode single-photon-sensitive avalanche photodiodes for GHz-rate near-infrared quantum communications," 2008 IEEE Military Communications Conference (MILCOM 2008), 1-6 (2008)
- [7] Oh, J., Wagner, J., Trippe, S., Lee, T., Lee, B., and Kim, C. H., "SIRIUS: a prototype astronomical intensity interferometer using avalanche photodiodes in linear mode," *Mon. Not. R. Astron. Soc.*, 500(4), 5630–5638 (2021)
- [8] Fields, R., Sun, X., Abshire, J. B., Beck, J., Rawlings, R. M., Sullivan, W., and Hinkley, D., "A linear mode photon-counting (LMPC) detector array in a CubeSat to enable earth science LiDAR measurements," 2015 IEEE International Geoscience and Remote Sensing Symposium (IGARSS 2015), 5312-5315 (2015)

- [9] Zayer, I., Sodnik, Z., Daddato, R., Lanucara, M., Schulz, K.-J., Smit, H., Sans, M., Becker, P., Giggenbach, D., Mata-Calvo, R., Fuchs C., and Rothman, J., "Lunar Optical Communications Link Demonstration Between NASA's Ladee Spacecraft and ESA's Optical Ground Station," SpaceOps 2014 Conference, AIAA 2014-1919, (2014)
- [10] Rothman, J., Pes, S., Bleuet, P., Abergel, J., Gout, S., Nicolas, J.-A., Rostaing, J.-P., Renet, S., Mathieu L., and Le Perchec, J., "Meso-photon detection with HgCdTe APDs at high count rates," J. Electron. Mater. 49, 6881–6892 (2020)
- [11] Sullivan, W., Beck, J., Scritchfield, R., Skokan, M., Mitra, P., Sun, X., Abshire, J., Carpenter, D., and Lane, B., "Linear-Mode HgCdTe Avalanche Photodiodes for Photon-Counting Applications," J. Electron. Mater. 44, 3092-3101 (2015)
- [12] Sun, X., Abshire, J. B., Beck, J. D., Mitra, P., Reiff, K., and Yang, G., "HgCdTe avalanche photodiode detectors for airborne and spaceborne lidar at infrared wavelengths," Opt. Express 25(14), 16589-16602 (2017)
- [13] Rothman, J., "Physics and Limitations of HgCdTe APDs: A Review," J. Electron. Mater. 47, 5657–5665 (2018)
- [14] Sodnik, Z., Heese, C., Arapoglou, P.-D., Schulz, K.-J., Zayer, I., Daddato, R., and Kraft, S., "Deep-space Optical Communication System (DOCS) for ESA's Space Weather mission to Lagrange orbit L5," 2017 IEEE International Conference on Space Optical Systems and Applications (ICSOS 2017), 28-33 (2017)
- [15] Sodnik, Z., Heese, C., Arapoglou, P.-D., Schulz, K.-J., Zayer, I., and Daddato, R., "European deep-space optical communication program," Proc. SPIE 10524, 105240Q (2018)
- [16] Agrawal, G. P., Fiber-Optic Communication Systems, 4th Ed., John Wiley & Sons, Hoboken, 166-167 (2010)